DOI: 10.1002/asia.201402224

Mesoporous Spherical $Li_4Ti_5O_{12}$ as High-Performance Anodes for Lithium-Ion Batteries

Guojun Du,[a, b] Zhaolin Liu,*[a] Siok Wei Tay,[a] Xiaogang Liu,*[a, b] and Aishui Yu[c]

Abstract: Porous microspherical $Li_4Ti_5O_{12}$ aggregates (LTO-PSA) can be successfully prepared by using porous spherical TiO_2 as a titanium source and lithium acetate as a lithium source followed by calcinations. The synthesized LTO-PSA possess outstanding morphology, with nanosized, porous, and spherical distributions, that allow good electrochemical performances, including high reversible capacity, good cycling stability, and impressive rate capacity, to be achieved. The specific capacity of the LTO-PSA at 30 C is as high as 141 $mA\,h\,g^{-1}$, whereas that of normal $Li_4Ti_5O_{12}$ powders prepared by a sol–gel method can only achieve 100 $mA\,h\,g^{-1}$. This improved rate performance can be ascribed to small $Li_4Ti_5O_{12}$ nanocrystallites, a three-dimensional mesoporous structure, and enhanced ionic conductivity.

Keywords: aggregates · electrochemistry · lithium-ion battery · mesoporous materials · nanoparticles

Introduction

Lithium-ion batteries (LIBs) are regarded as promising new power sources for hybrid electric vehicles (HEVs) and electric vehicles (EVs), as well as for portable electronic devices, owing to their long cycle life and high energy density. However, current LIBs with graphite as the anodic material cannot meet the stringent requirements for high-power applications owing to poor rate performance and safety concerns.[1–3] The lithium-ion intercalation voltage of graphite is close to the lithium electroplating potential, which could cause serious safety issues.[4,5] Therefore, a key solution for these challenges is to use an electrochemical redox couple with higher equilibrium potentials, which makes lithium dendrite formation thermodynamically less favorable. Spinel $Li_4Ti_5O_{12}$, with the Ti^{4+}/Ti^{3+} redox couple working at approximately 1.55 V versus Li^+/Li, meets this requirement. However, spinel $Li_4Ti_5O_{12}$ suffers from poor electrical conductivity and a low lithium diffusion coefficient, which lead to a suppressed rate capability.[6,7]

So far, many strategies have been reported for enhancing the rate capability of $Li_4Ti_5O_{12}$, which include 1) enhancing the electronic conductivity by doping or surface modification and 2) reducing the particle size and increasing the surface area.[8–14] In particular, the morphology of $Li_4Ti_5O_{12}$ has a great influence on its electrochemical properties; thus affecting the battery performance. Nanostructured $Li_4Ti_5O_{12}$ with various morphologies can enhance kinetic performance by reducing the transport length of lithium ions and electrons.[6,7,13–19] Among nanostructured $Li_4Ti_5O_{12}$, spherical morphology shows great advantages, such as lower interfacial energy, high volumetric energy density, and better fluidity characteristics,[16–19] which can favor improved battery performance. In addition, an electrode consisting of nanocrystalline $Li_4Ti_5O_{12}$ with three-dimensional (3D) porosity is appealing because it can provide fast electronic conduction in the solid phase and ion conduction at reasonable rates in both solid and liquid phases. Therefore, we reason that the employment of mesoporous spherical $Li_4Ti_5O_{12}$ to LIBs can enhance their performance.

Herein, we report, for the first time, a strategy for the synthesis of porous microspherical $Li_4Ti_5O_{12}$ aggregates (LTO-PSA) for high-performance LIBs by using porous spherical TiO_2 (TiO_2-PS) as the titanium source and lithium acetate as the lithium source. Synthesized LTO-PSA possess outstanding morphology, with nanosized, porous, and spherical distribution, that achieve good electrochemical performances. Further application of LTO-PSA in LIBs exhibits good reversible capacity, cycling stability, and rate capacity.

[a] G. Du, Dr. Z. Liu, Dr. S. W. Tay, Prof. X. Liu
Institute of Materials Research and Engineering
Agency for Science, Technology and Research (A*STAR)
3 Research Link, 117602 (Singapore)
Fax: (+65) 68720785
E-mail: zl-liu@imre.a-star.edu.sg

[b] G. Du, Prof. X. Liu
Department of Chemistry
National University of Singapore
3 Science Drive 3, 117543 (Singapore)
E-mail: chmlx@nus.edu.sg

[c] Prof. A. Yu
Department of Chemistry, Shanghai Key Laboratory
of Molecular Catalysis and Innovative Materials
Institute of New Energy, Fudan University
Shanghai 200438 (P.R. China)

Supporting information for this article is available on the WWW under http://dx.doi.org/10.1002/asia.201402224.

Results and Discussion

The preparation process for LTO-PSA is illustrated in Scheme 1. TiO_2-PS was prepared through self-organization from ultrathin TiO_2 nanosheets, as reported in the literature.[20] Subsequently, as-prepared TiO_2 was submerged in a solution of lithium acetate. Finally, the lithium acetate impregnated porous TiO_2 powder was heat-treated at 700 °C for 2 h in argon to form crystallized $Li_4Ti_5O_{12}$ aggregates.

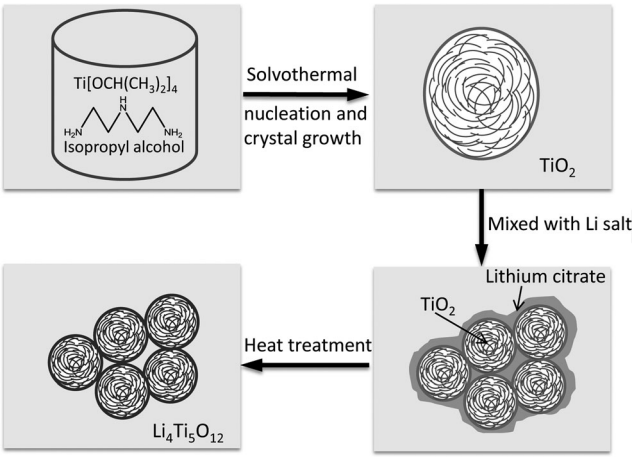

Scheme 1. Synthetic process of the preparation of LTO-PSA.

The morphology of as-prepared TiO_2 and $Li_4Ti_5O_{12}$ was characterized by field-emission scanning electron microscopy (FESEM) and high-resolution transmission electron microscopy (HRTEM), as shown in Figure 1. In Figure 1 a and b, both TiO_2 and LTO-PSA show microspherical morphologies with an average diameter of 1.5 μm and good uniformity. The constituent nanosheets are clearly visible and adopt random orientations. Generally, TiO_2 nanosheets are easy to form in the presence of a certain concentration of diethylenetriamine (DETA) in the solvothermal synthetic system. Large ultrathin TiO_2 nanosheets are highly flexible and can readily self-organize into different hierarchical architectures.[20] Adsorption of the lithium salt on porous TiO_2 spheres followed by thermal treatment (in argon gas at 700 °C for 2 h) to form crystallized $Li_4Ti_5O_{12}$ aggregates did not result in significant morphological changes (Figure 1 b). A high-magnification image of LTO-PSA clearly demonstrates that the entire sphere is composed of numerous nanosheets (Figure 1 c). HRTEM analysis was employed to determine the crystal facets. Figure 1 d shows a HRTEM image of LTO-PSA, and a lattice spacing of 0.481 nm corresponding to the (111) plane of spinel $Li_4Ti_5O_{12}$ can be observed.

Figure 2 a shows X-ray diffraction (XRD) patterns of TiO_2-PS and LTO-PSA. For the TiO_2 sample, all of the identified peaks can be perfectly assigned to anatase TiO_2 (space group $I41/amd$, $a = 3.785$ Å, $c = 9.514$ Å, JCPDS card no. 21-1272). For the LTO-PSA sample, phase-pure $Li_4Ti_5O_{12}$ was obtained, as demonstrated by all peaks in the XRD pattern of the product being well indexed as spinel $Li_4Ti_5O_{12}$ (space group $Fd3m$, $a = 8.356$ Å, JCPDS card no. 49-0207). The sharp diffraction peaks imply that the obtained TiO_2 and

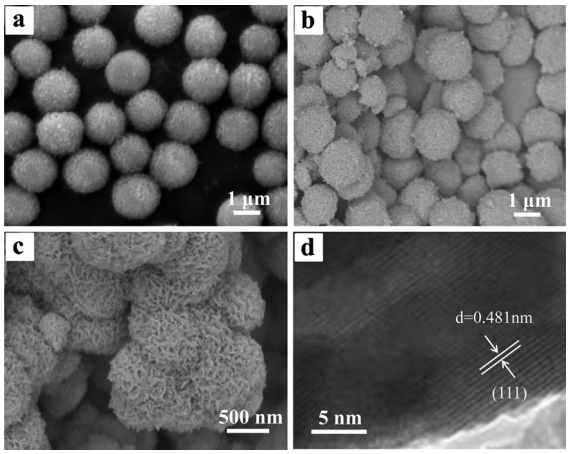

Figure 1. SEM images of the porous microspheres of TiO_2 (a) and LTO-PSA (b). c) High-magnification SEM image of LTO-PSA. d) HRTEM image of individual LTO-PSA.

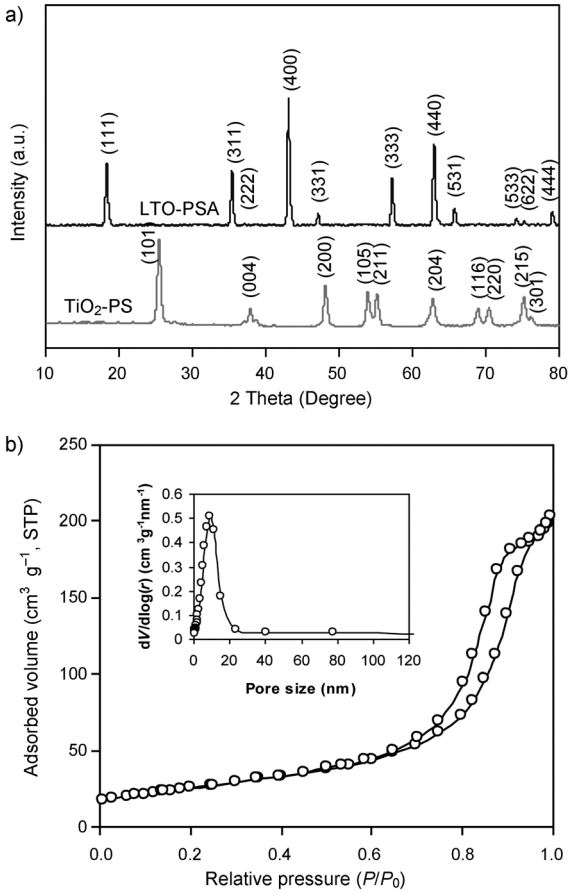

Figure 2. a) XRD patterns of TiO_2-PS and LTO-PSA. b) The N_2 adsorption/desorption isotherm of LTO-PSA; the inset shows the corresponding pore size distributions of LTO-PSA.

$Li_4Ti_5O_{12}$ are well crystallized. Nitrogen sorption isotherms were generated to investigate the porous structure and BET surface areas of LTO-PSA (Figure 2b). It can be seen that the adsorption isotherm of LTO-PSA is of type IV, according to IUPAC classification, which is indicative of mesoporous material. The remarkable nitrogen uptake above a relative pressure of 0.65 is due to capillary condensation of nitrogen in the mesoporous texture. The inset of Figure 2b shows the pore size distribution curve derived from the Barrett–Joyner–Halenda (BJH) method, which indicates that the pore size of LTO-PSA is centered at around 10 nm. The specific surface area and pore volume of LTO-PSA are 92 $m^2 g^{-1}$ and 0.31 $cm^3 g^{-1}$, respectively. It is speculated that the increase in pore volume is related to cross-linking between nanosheets, which facilitates lithium transportation during cycling.

X-ray photoelectron spectroscopy (XPS) was used to confirm the chemical state of the ions in LTO-PSA. Detailed scanning spectra for LTO-PSA are given in Figure 3. The Ti

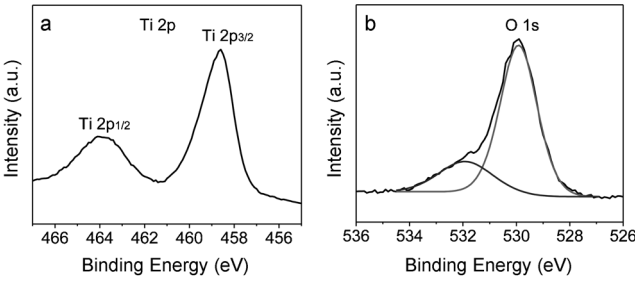

Figure 3. XPS analysis of Ti 2p (a) and O 1s (b) for LTO-PSA.

2p signal of the $Li_4Ti_5O_{12}$ spinel shows a Ti $2p_{3/2}$ peak centered at 458.3 eV and a Ti $2p_{1/2}$ peak at 464.1 eV (Figure 3a). The observed binding energies of the Ti $2p_{3/2}$ and Ti $2p_{1/2}$ values are in good agreement with literature values;[5,21] this indicates that the oxidation state of titanium cations in the sample of $Li_4Ti_5O_{12}$ could be recognized as Ti^{4+}. The O 1s photoelectron core-level spectrum is shown in Figure 3b. The spectrum exhibits the main peak at a binding energy of 530.0 eV, which is derived from oxygen associated to Ti–O in the synthesized material.[22] The peak at 532.0 eV can be attributed to oxygen and water molecules absorbed on the surface of the compound.

To test the potential application of LTO-PSA in LIBs, we investigated their electrochemical performance toward lithium insertion/extraction. For comparison, $Li_4Ti_5O_{12}$ powders (LTO-SG) were also prepared by a sol–gel method following a previous report.[23] Figure 4a displays the charge/discharge curves of LTO-PSA cycled at various current rates from 1 to 70 C. It can be found that the LTO-PSA exhibit very high capacity. A specific discharge capacity of 168 mA h g^{-1} is observed when the LTO-PSA are discharged at 1 C; for discharge rates of 10, 20, 30, and 50 C, the specific discharge capacities are 159, 151, 141, and 113 mA h g^{-1}, respectively. Figure 4b shows a comparison of the rate capa-

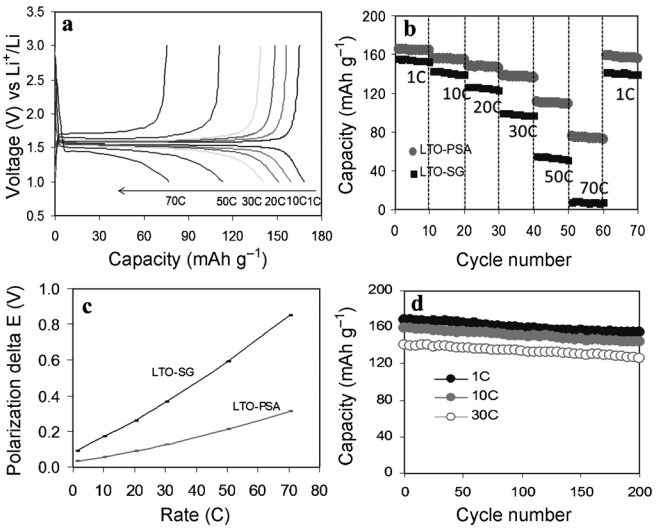

Figure 4. a) Charge/discharge curves of LTO-PSA cycled at various current rates. b) The rate and cycling performances of LTO-PSA and LTO-SG. c) Plots of ΔE versus C rates. d) Cycling performance of LTO-PSA.

bilities of LTO-PSA and LTO-SG at different rates. The discharge specific capacities of LTO-SG decrease significantly from 1 to 70 C, whereas that of LTO-PSA decreases much more slowly at the same rate. Remarkably, at the highest rate of 70 C, LTO-PSA still deliver a capacity of 77 mA h g^{-1}, which is much higher than that of LTO-SG (ca. 8 mA h g^{-1}).

Figure 4c displays the polarization of ΔE versus rate plots of the LTO-PSA and LTO-SG electrodes. The values of ΔE are defined as the differences between the potentials of charge and discharge plateaus. The two curves exhibit a pseudo-linear ohmic-loss behavior. The larger slope means more charge-transfer resistance, which causes the relatively low rate capacity. This result is in good agreement with the results given in Figure 4b.

To demonstrate the excellent cycling stability, long cycling tests of the LTO-PSA electrode under 1, 10, and 30 C were examined and the results are given in Figure 4d. The initial discharge capacities of the LTO-PSA at 1, 10, and 30 C are 168, 159, and 141 mA h g^{-1}, respectively, and the retained discharge capacities after 200 cycles are 154, 144, and 126 mA h g^{-1}. The capacity retention ratios for 1, 10, and 30 C are 91.7, 90.6, and 89.4%, respectively. As a result, LTO-PSA exhibits an outstanding cycling performance.

To clarify the origin of the excellent rate capability and cycling properties of LTO-PSA, electrochemical impedance spectroscopy (EIS) experiments for the LTO-PSA and LTO-SG electrodes were performed (Figure 5a). The EIS results were simulated by Z-view software with the equivalent circuit shown in the inset of Figure 5a. According to the equivalent circuit, the intercept at the Z' axis at high frequency is attributed to the ohmic resistance (R_o), which represents the resistance of the electrode and electrolyte. The semicircle in the middle frequency range is associated with the charge-transfer resistance (R_{ct}) and the constant phase element

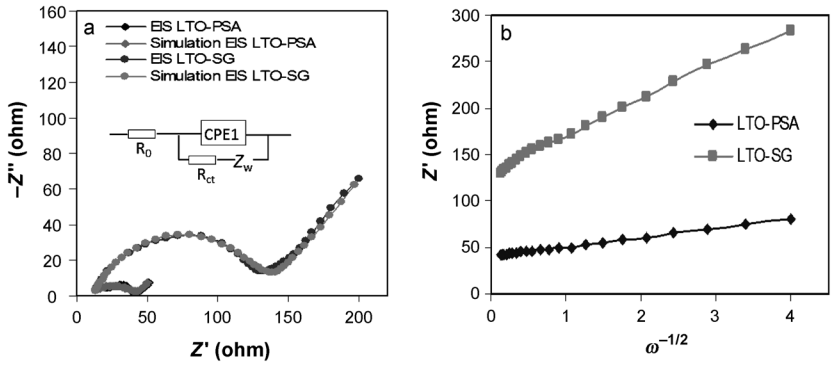

Figure 5. a) EIS experiments for LTO-PSA and LTO-SG. The inset shows the equivalent circuit for the plot fitting. b) Relationship between real impedance and $\omega^{-1/2}$ for LTO-PSA and LTO-SG.

(CPE). The CPE is used to take into account the roughness of the particle surface instead of a double-layer capacitance (C_d).[24–26] The slope line at low frequency corresponds to the Warburg impedance (Z_w), which is related to lithium-ion diffusion within the particles. Figure 5a shows that the R_o of LTO-PSA is similar to that of LTO-SG, and indicates that the electronic conductivity of both electrodes is almost the same. In contrast, the R_{ct} (36.7 Ω) of LTO-PSA is much less than that (124.8 Ω) of LTO-SG, which indicates that LTO-PSA may aid in reducing polarization.

To further study lithium-ion diffusion within the particles, the profiles of the real axis (Z') versus the reciprocal square root of the lower angular frequencies ($\omega^{-1/2}$) were plotted (Figure 5b). It should be noted that lithium-ion diffusion within the particles here can be ascribed to Warburg diffusion. According to the relationship between the real axis and the reciprocal square root of the lower angular frequencies [Eq. (1)], and the definition of diffusion coefficients [Eq. (2)], the diffusion coefficients (D) of the lithium ion diffusing into the bulk electrode materials can be calculated.[27]

$$Z' = R_o + R_{ct} + \sigma_w \omega^{-1/2} \quad (1)$$

$$D = R^2T^2/2A^2F^4C^2{\sigma_w}^2 \quad (2)$$

in which R is the ideal gas constant; T is the absolute temperature; A is the surface area of the electrode; F is the Faraday constant; C is the concentration of lithium ion; and σ_w is the Warburg factor, which is obtained from the slope of Z' versus the reciprocal square root of the lower angular frequencies ($\omega^{-1/2}$; Figure 5b).

As can be clearly seen from the results given in Table 1, the value of D for LTO-PSA is about 12 times larger than that of LTO-SG. Therefore, we believe that the 3D mesoporous structure and numerous small $Li_4Ti_5O_{12}$ nanosheets can facilitate the fast transfer of lithium ions and electrons. In addition, the presence of abundant mesopores also provide a large surface area, which increases the electrolyte–electrode contact area and leads to a decrease in the current density per unit surface area and an increase in the charge–discharge rate.[7,28] Numerous small $Li_4Ti_5O_{12}$ nanosheets can facilitate lithium-ion and electron transfer in nanostructured electrodes relative to the LTO-SG particles, which are larger with fewer pores (see Figure S1 in the Supporting Information).

For the LIB electrodes, during charging and discharging electrical energy by intercalation and deintercalation of lithium ions and electrons, the electrons and lithium ions must reach or leave the reaction point in the active material simultaneously. Thus, the active material, with an excellent rate charge and discharge performance, must have both high electronic and ionic conductivity. The simulated results for the LTO-PSA particles suggest that the transport number of the lithium ion can satisfy the reaction requirement at high charge and discharge rates.

Table 1. Simulation results for the EIS experiments shown in Figure 5.

Samples	R_o [Ω][a]	R_{ct} [Ω][b]	σ_w [Ω cm^2 s$^{-0.5}$][c]	D [cm^2 s^{-1}][d]
LTO-PSA	7.6	36.7	11.1	2.81×10^{-10}
LTO-SG	7.9	124.8	39.1	2.30×10^{-11}

[a] Ohmic resistance. [b] Charge-transfer resistance. [c] The Warburg factor. [d] The diffusion coefficients of lithium ions.

We also compared our results with those reported in the literature. The results for LTO-PSA at these high rates are better than those of Xia et al.[29] and Duh et al.,[30] who also demonstrated that meso- or nanoporous architectures could effectively improve electrode rate performance. The greatly enhanced rate capability may be attributed to the 3D mesoporous structure and small $Li_4Ti_5O_{12}$ nanocrystallites, which result in better ionic conduction throughout the electrode.

Conclusion

In this research, LTO-PSA have been successfully prepared from TiO_2-PS as a titanium source and lithium acetate as a lithium source followed by calcinations. The synthesized LTO-PSA microspheres exhibited excellent electrochemical profiles, including high reversible capacity, good cycling stability, and impressive rate capacity. The specific capacity of LTO-PSA at 30 C was as high as 141 mA h g^{-1}, whereas that of normal LTO-SG could only achieve 100 mA h g^{-1}. At the highest rate of 70 C, LTO-PSA still delivered a capacity of 77 mA h g^{-1}, which was much higher than that of LTO-SG (ca. 8 mA h g^{-1}).

Further studies revealed that the 3D mesoporous structure and small $Li_4Ti_5O_{12}$ nanocrystallites resulted in better ionic conduction throughout the electrode. These two factors, coupled with the de-aggregation of $Li_4Ti_5O_{12}$ microspherical particles, were responsible for the great improvement in electrochemical properties.

High-performance $Li_4Ti_5O_{12}$ could be a promising anode material in LIBs for EVs in the future.

Experimental Section

Synthesis of TiO_2-PS and LTO-PSA

Isopropanol (IPA), DETA, lithium citrate, and titanium(IV) isoproxide (TIP) were purchased from Sigma–Aldrich. All chemicals were used without further purification.

The samples of TiO_2-PS were prepared by using a method previously reported.[20] In a typical synthesis, DETA (0.05 mL) was added to IPA (70 mL). After the solution was stirred for a few minutes, TIP (2.5 mL) was added. The solution was then transferred to a 100 mL Teflon-lined stainless-steel autoclave and kept in an oven at 200 °C for 24 h. The white precipitate was obtained by centrifugation, washed thoroughly with ethanol, and dried at 60 °C overnight. The product was calcined at 450 °C for 2 h with a heating rate of 1 °C min^{-1} to obtain a highly crystalline anatase phase.

A stoichiometric amount of lithium citrate was dissolved in deionized water (20 mL), and subsequently, a stoichiometric amount of TiO_2-PS was added to the solution and stirred for 1 h. The mixture was then heated at 60 °C for 24 h, followed by calcination at 700 °C for 2 h under argon to obtain LTO-PSA. For comparison, the LTO-SG was also prepared by a sol–gel method following a previously published procedure.[22] Details can be seen in the Supporting Information.

Structural and Electrochemical Characterization

The morphologies of LTO-PSA and TiO_2-PS were observed under a field-emission scanning electron microscope (JEOL JSM 6700) at an accelerating voltage of 5 kV and a TEM (Philips CM300) at 300 kV. XRD measurements were performed by using a Bruker D8 Discover GADDS X-ray diffractometer with $Cu_{K\alpha}$ radiation. XPS data were recorded with a Theta Probe electron spectrometer from Thermo Scientific by using $Al_{K\alpha}$ ($h\nu = 1484.6$ eV) radiation. The binding energies were corrected by the C 1s line at 285.0 eV from adventitious carbon. Nitrogen adsorption and desorption isotherms at 77.3 K were obtained with a NOVA 1000 surface area–pore size analyzer. The BET surface area was calculated from experimental points measured at a relative pressure of $P/P_o = 0.05$–0.35. The pore size distribution was calculated by the BJH method.

For the preparation of working electrodes, LTO-PSA or LTO-SG (80 wt %) were blended with 10 wt % carbon black and 10 wt % poly(vinylidene difluoride) (PVDF) in 1-methyl-2-pyrrolidinone (NMP) to form a slurry. The slurry was spread onto copper foil from a doctor blade, followed by drying in a vacuum oven at 120 °C overnight. The loading of $Li_4Ti_5O_{12}$ on the working electrode was about 4 mg. Each coated electrode was assembled into a Swagelok Cell by using lithium as the counter electrode, microporous polypropylene (Celgard 2325, USA) as the separator, and 1 M $LiPF_6$ in a 50:50 (w/w) mixture of ethylene carbonate (EC) and diethyl carbonate (DEC) as the electrolyte. Cell assembly was performed in an argon-filled glove box with less than 1 ppm each of oxygen and moisture. Cycle life and rate capacity was measured by using a battery test system (MACCOR 4200) at a voltage range of 3.0–1.0 V(vs. Li^+/Li). The EIS study was conducted by using an Autolab electrochemical workstation under the frequency range of 10^5–10^{-2} Hz. All electrochemical measurements were performed at room temperature.

Acknowledgements

This research was supported by the Institute of Materials Research and Engineering of the Agency for Science, Technology, and Research, Singapore through the research grant IMRE/11-1C0218 and IMRE/12-2P0503.

[1] J. M. Tarascon, M. Armand, *Nature* **2001**, *414*, 359–367.
[2] B. K. Guo, X. Q. Wang, P. F. Fulvio, M. F. Chi, S. M. Mahurin, X. G. Sun, S. Dai, *Adv. Mater.* **2011**, *23*, 4661–4666.
[3] S. B. Yang, X. L. Feng, K. Müllen, *Adv. Mater.* **2011**, *23*, 3575–3579.
[4] K. Amine, I. Belharouak, Z. H. Chen, T. Tran, H. Yumoto, N. Ota, S. T. Myung, Y. K. Sun, *Adv. Mater.* **2010**, *22*, 3052–3057.
[5] M. R. Jo, K. M. Nam, Y. Lee, K. Song, J. T. Park, Y. M. Kang, *Chem. Commun.* **2011**, *47*, 11474–11476.
[6] K. M. Yang, Y. N. Ko, J. Y. Yun, Y. C. Kang, *Chem. Asian J.* **2014**, *9*, 443–446.
[7] L. F. Shen, X. G. Zhang, E. Uchaker, C. Z. Yuan, G. Z. Cao, *Adv. Energy Mater.* **2012**, *2*, 691–698.
[8] T. F. Yi, L. J. Jiang, J. Shu, C. B. Yue, R. S. Zhu, H. B. Qiao, *J. Phys. Chem. Solids* **2010**, *71*, 1236–1242.
[9] J. Y. Lin, C. C. Hsu, H. P. Ho, S. H. Wu, *Electrochim. Acta* **2013**, *87*, 126–132.
[10] A. Sivashanmugam, S. Gopukumar, R. Thirunakaran, C. Nithya, S. Prema, *Mater. Res. Bull.* **2011**, *46*, 492–500.
[11] J. Liu, X. F. Li, M. Cai, R. Y. Li, X. L. Sun, *Electrochim. Acta* **2013**, *93*, 195–201.
[12] Y. Q. Wang, L. Gu, Y. G. Guo, H. Li, X. Q. He, S. Tsukimoto, Y. Ikuhara, L. J. Wan, *J. Am. Chem. Soc.* **2012**, *134*, 7874–7879.
[13] L. F. Shen, E. Uchaker, X. G. Zhang, G. Z. Cao, *Adv. Mater.* **2012**, *24*, 6502–6506.
[14] S. C. Lee, S. M. Lee, J. W. Lee, J. B. Lee, S. M. Lee, S. S. Han, H. C. Lee, H. J. Kim, *J. Phys. Chem. C* **2009**, *113*, 18420–18423.
[15] L. J. Xi, H. K. Wang, S. L. Yang, R. G. Ma, Z. G. Lu, C. W. Cao, K. L. Leung, J. Q. Deng, A. L. Rogach, C. Y. Chung, *J. Power Sources* **2013**, *242*, 222–229.
[16] J. Gao, C. Y. Jiang, J. R. Ying, C. R. Wan, *J. Power Sources* **2006**, *155*, 364–367.
[17] L. Zhao, Y. S. Hu, H. Li, Z. X. Wang, L. Q. Chen, *Adv. Mater.* **2011**, *23*, 1385–1388.
[18] Y. F. Tang, L. Yang, Z. Qiu, J. S. Huang, *J. Mater. Chem.* **2009**, *19*, 5980–5984.
[19] Y. Y. Zhao, S. P. Pang, C. J. Zhang, Q. H. Zhang, L. Gu, X. H. Zhou, G. C. Li, G. L. Cui, *J. Solid State Electrochem.* **2013**, *17*, 1479–1485.
[20] J. S. Chen, Y. L. Tan, C. M. Li, Y. L. Cheah, D. Luan, S. Madhavi, F. Y. C. Boey, L. A. Archer, X. W. Lou, *J. Am. Chem. Soc.* **2010**, *132*, 6124–6130.
[21] M. Oku, K. Wagatsuma, S. Kohiki, *Phys. Chem. Chem. Phys.* **1999**, *1*, 5327–5331.
[22] T. Z. Yang, C. M. Shen, H. T. Yang, C. W. Xiao, Z. C. Xu, S. T. Chen, D. X. Shi, H. J. Gao, *Surf. Interface Anal.* **2006**, *38*, 1063–1067.
[23] N. Q. Zhang, Z. M. Liu, T. Y. Yang, C. L. Liao, Z. J. Wang, K. N. Sun, *Electrochem. Commun.* **2011**, *13*, 654–656.
[24] F. Nobili, R. Tossici, F. Croce, B. Scrosati, R. Marassi, *J. Power Sources* **2001**, *94*, 238–241.
[25] M. Umeda, K. Dokko, Y. Fujita, M. Mihamedi, I. Uchida, J. R. Selman, *Electrochim. Acta* **2001**, *47*, 885–890.
[26] G. T. K. Fey, W. H. Yo, Y. C. Chang, *J. Power Sources* **2002**, *105*, 82–86.
[27] A. Y. Shenouda, H. K. Liu, *J. Alloys Compd.* **2009**, *477*, 498–503.
[28] Y. G. Guo, Y. S. Hu, W. Sigle, J. Maier, *Adv. Mater.* **2007**, *19*, 2087–2091.
[29] G. N. Zhu, H. J. Liu, J. H. Zhuang, C. X. Wang, Y. G. Wang, Y. Y. Xia, *Energy Environ. Sci.* **2011**, *4*, 4016–4022.
[30] Y. S. Lin, M. C. Tsai, J. G. Duh, *J. Power Sources* **2012**, *214*, 314–318.

Received: March 13, 2014
Published online: June 6, 2014

